THE ASTROPHYSICAL JOURNAL, 471:643–656, 1996 November 10

HUBBLE SPACE TELESCOPE OBSERVATIONS OF THE LENSING CLUSTER ABELL 2218

J.-P. KNEIB,[1] R. S. ELLIS,[1] I. SMAIL,[2] W. J. COUCH,[3] AND R. M. SHARPLES[4]

Received 1995 November 2; accepted 1996 June 13

ABSTRACT

We present a striking new *Hubble Space Telescope* (*HST*) observation of the rich cluster Abell 2218 taken with the Wide Field Planetary Camera 2. *HST*'s restored image quality reveals a sizable number of gravitationally lensed features in this cluster, significantly more than had been identified by using ground-based telescopes. The brightest arcs are resolved by *HST* and show internal features that enable us to identify multiply imaged examples, confirming and improving the mass models of the cluster determined from ground-based observations. Although weak lensing has been detected statistically in this and other clusters from ground-based data, the superlative resolution of *HST* enables us to individually identify weakly distorted images more reliably than hitherto, with important consequences for their redshift determination. Using an improved mass model for the cluster calibrated with available spectroscopy for the brightest arcs, we demonstrate how inversion of the lensing model can be used to yield the redshift distribution of ~ 80 faint arclets to $R \simeq 25$. We present a new formalism for estimating the uncertainties in this inversion method and review prospects for interpreting our results and verifying the predicted redshifts.

Subject headings: cosmology: observations — galaxies: clusters: individual (Abell 2218) — gravitational lensing

1. INTRODUCTION

The gravitational lensing of faint background galaxies by rich clusters is emerging as a very promising method to constrain both the distribution of dark matter in clusters and the statistical redshift distribution of galaxies beyond the reach of conventional spectrographs (Fort & Mellier 1994). The lensing distortion induced in the image of a typical distant galaxy by a foreground rich cluster depends upon the product of a scale factor (involving the galaxy and cluster redshifts and the adopted cosmological model) and the second derivatives of the projected cluster potential (Schneider, Ehlers, & Falco 1992). The majority of the faint lensed images are only weakly distorted, and these are termed "arclets." However, a small fraction are highly distorted "giant arcs"—images that lie near critical lines and suffer high amplification. These are particularly helpful in mass modeling since their relatively bright magnitudes mean that they can often be studied spectroscopically. With redshifts for one or more giant arcs in a cluster, the absolute mass of the central regions can be accurately determined. Multiply imaged sources, even without redshifts, provide additional information on the geometrical configuration of the potential well in the core regions (Mellier, Fort, & Kneib 1993; Smail et al. 1995a). Recent work has concentrated on clusters with arcs of known redshift *and* multiply imaged sources. In such cases, a robust model of the cluster mass can be constructed, allowing inversion of the lens equations for the arclet population and yielding the redshift distribution of extremely faint galaxies.

For the well-studied cluster Abell 370 ($z_{cl} = 0.37$), Kneib et al. (1994a) demonstrated a first application of this inversion technique by identifying ~ 30 candidate arclets with axial ratios $a/b \gtrsim 1.4$ from ground-based images taken in superlative conditions. For each arclet, unlensed magnitudes and probable redshifts to a limit of $B \simeq 27$ were inferred from a detailed mass model calibrated by the redshift of a giant arc and the properties of various multiple images (Kneib et al. 1993). However, this new technique suffered from several uncertainties. First, simple mass models may ignore substructure in the cluster mass distribution, leading to imprecise inversion. Second, in the absence of spectroscopic or morphological data, some of the candidate multiply imaged objects used to model the form of the potential may be spuriously identified in ground-based data. Finally, even in the best ground-based conditions, the limited angular resolution makes it difficult to distinguish lensed arclets from intrinsically elongated faint sources and to accurately measure their shapes; such confusion may lead to contamination of the inverted redshift distribution by cluster members, foreground spirals, and close galaxy pairs.

Even in its aberrated state, the advantages of the *Hubble Space Telescope* (*HST*) for lensing studies over the best ground-based telescopes soon became evident (Smail et al. 1996). Here we illustrate that the refurbished *HST* is even more powerful, allowing reliable identification of multiple images and faint arclets. Considerable progress is thus possible with *HST* in the inversion method developed by Kneib et al. (1994a).

A plan of the paper follows. Section 2 describes the observations and gives a qualitative description of the *HST* images, including those lensed features that allow us to improve the ground-based model of Kneib et al. (1995). Section 3 describes the improved mass model we have implemented. Starting from the mass model of a cluster, § 4 introduces the theory of the lens inversion and discusses the probability distribution of the redshift of a sheared galaxy. The sources of uncertainty in this inversion are also discussed in the context of observational data. In § 5, we present our results on the faint field galaxy redshift distribu-

[1] Institute of Astronomy, Madingley Road, Cambridge CB3 0HA, England.
[2] The Observatories of the Carnegie Institution of Washington, 813 Santa Barbara Street, Pasadena, CA 91101-1292.
[3] School of Physics, University of New South Wales, Sydney, NSW 2052, Australia.
[4] Department of Physics, University of Durham, South Road, Durham DH1 3LE, England.

tion and discuss the limitations of comparing such results with model predictions as well as the prospects for verifying the inverted redshifts with further observations. Section 6 summarizes the overall conclusions of the paper. Throughout, we assume $H_0 = 50$ km s^{-1} Mpc^{-1}, $\Omega_0 = 1$, and $\Lambda = 0$.

2. OBSERVATIONS AND ANALYSIS

2.1. *Previous Observations of Abell 2218*

Abell 2218 (Fig. 1*a* [Pl. 8]) is one of the best studied rich clusters at intermediate redshift ($z_{cl} = 0.175$). Le Borgne, Pelló, & Sanahuja (1992) presented a detailed photometric and spectroscopic survey of the cluster and derived a rest-frame velocity dispersion of $\sigma_{cl} = 1370^{+160}_{-120}$ km s^{-1}, indicative of a deep potential well. This is supported by a high X-ray luminosity [$L_X(0.5\text{–}4.4\ \text{keV}) = 6.5 \times 10^{44}$ ergs s^{-1}] and a strong Sunyaev-Zeldovich decrement (Jones et al. 1993; Birkinshaw & Hughes 1994). The cluster contains a number of luminous giant arcs, discovered and extensively studied by Pelló et al. (1988, 1992). Several of the brighter arcs have been observed spectroscopically; redshifts for these and ground-based colors for other lensed features provide the basic ingredients for the recent mass model of Kneib et al. (1995). Using four systems of arcs and possible counterarcs, tentatively identified from ground-based colors (Nos. 289, 359–328, 384–468, and 730, in the numbering scheme of Le Borgne et al. 1992), Kneib et al. (1995) determined a mass distribution for the cluster core that is bimodal in form and concentrated around the two most luminous cluster galaxies (Nos. 391, 244; see Table 3 below). Furthermore, they made a first qualitative comparison with the *ROSAT* HRI map and claimed that the assumption of hydrostatic equilibrium was not applicable in the central region as a result of a recent merger, which could explain the small differences between the mass map and the X-ray map. In this paper, we do not revisit the X-ray data but primarily concentrate on the verification and refinement of the Kneib et al. mass model by using new *HST* data.

2.2. *HST Observations and Photometric Catalog*

Abell 2218 was observed by the *HST* Wide Field Planetary Camera 2 (WFPC2) camera on 1994 September 2. Three exposures totaling 6500 s were taken through the F702W filter. Each exposure was shifted relative to the others by 3 WFC pixels (0.″30), providing a partial overlap of the chip fields. After pipeline processing, standard IRAF STSDAS routines were employed to shift and combine the frames to remove both cosmic rays and hot pixels. We discarded the PC chip from our analysis because of its brighter isophotal limit. The final frame comprising the three WFC chips (Figs. 1*a*, 1*b* [Pl. 8–9]) has an effective resolution of 0.″14 and a 1 σ detection limit per resolution element of $R \simeq 30$. We convert our instrumental F702W magnitudes into standard R using the synthetic zero point and color corrections listed in Holtzman et al. (1995). For the color term, we choose $(V-R) \simeq 0.6$, typical of the faint field population (Smail et al. 1995c). The color correction is +0.2 mag, and the typical photometric errors of our faintest objects, $R < 25.5$, are $\delta R \sim 0.1$–0.2.

To produce a catalog of faint arclets from our data, we first analyzed the *HST* image by using the SEXTRACTOR package (Bertin 1995; Bertin & Arnouts 1996). All objects with isophotal areas above 12 pixels (0.12 arcsec^2) at the $\mu_R = 24.8$ mag arcsec^{-2} isophote (2 σ pixel^{-1}) were selected. A comparison of the differential number counts of these images to deep ground-based R-counts (Smail et al. 1995c) shows a marked excess of galaxies brighter than $R \sim 21.5$ due to cluster members (Fig. 2) and a steep rollover in the observed counts beyond $R \sim 25$ arising from an incompleteness that amounts to 55% in the $R = 25$–26 bin. We thus applied a magnitude limit of $R = 26$, yielding a total of 440 images over a 4.7 arcmin^2 area. A neural network algorithm (Bertin & Arnouts 1996; Bertin 1994) was used to separate stars and galaxies, leading to the exclusion of 25 starlike objects from the catalog.

From this list, we selected a sample of candidate arclets, first removing all galaxies with $R < 21.5$ (probable cluster members) and objects lying in the halos of giant elliptical galaxies and very faint objects ($R > 25$), as their photometry and shapes are uncertain. The procedure reduced our catalog to $\sim$235 arclet candidates.

2.3. *Multiply Imaged Features*

At this stage, it is useful to review the multiply imaged features identified on the *HST* image in the context of the ground-based predictions, prior to using them to improve the mass model of Kneib et al. (1995).

Four bright arcs and counterarcs were identified as matching images by Kneib et al. (1995) on the basis of their ground-based colors. Each of these is clearly resolved by *HST* with internal structures that enable us to verify their multiply imaged nature (see Fig. 1*c* of Smail et al. 1996). We discuss each of these images here and summarize their photometric properties in Table 1.

Nos. 384 and 468.—No. 384 is a most impressive arc system, with an internally symmetric pattern of unresolved knots, showing that this image is clearly formed from the

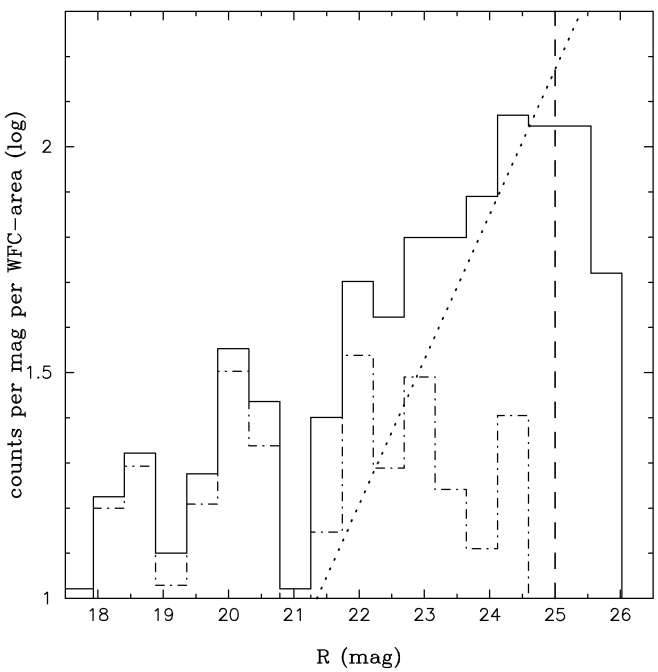

FIG. 2.—Differential galaxy counts within the Abell 2218 WFC image (4.7 arcmin^2). The dashed line defines our estimated completeness limit at the 55% level. The dotted line indicates field counts in R from Smail et al. (1995c). The dot-dashed line is the cluster galaxy counts, estimated by subtracting the field counts from the observed counts.

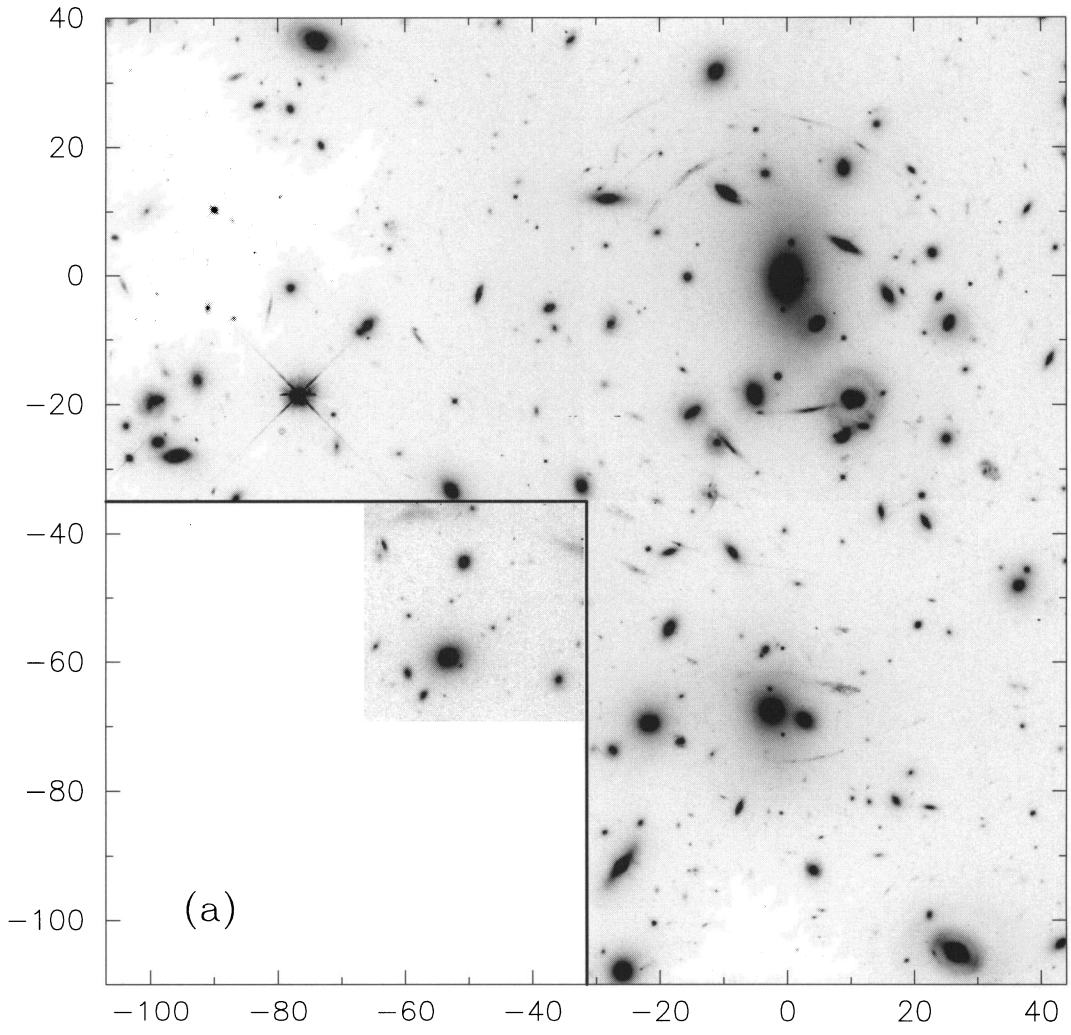

FIG. 1*a*

FIG. 1.—(*a*) Full field of our F702W WFPC2 exposure of Abell 2218 ($z = 0.175$). (*b*) Central portion, showing that several multiply imaged sources, numbered according to the scheme of Le Borgne et al. (1992), are confirmed by virtue of their mirrored morphological features (see text for details); scale is in arcseconds.

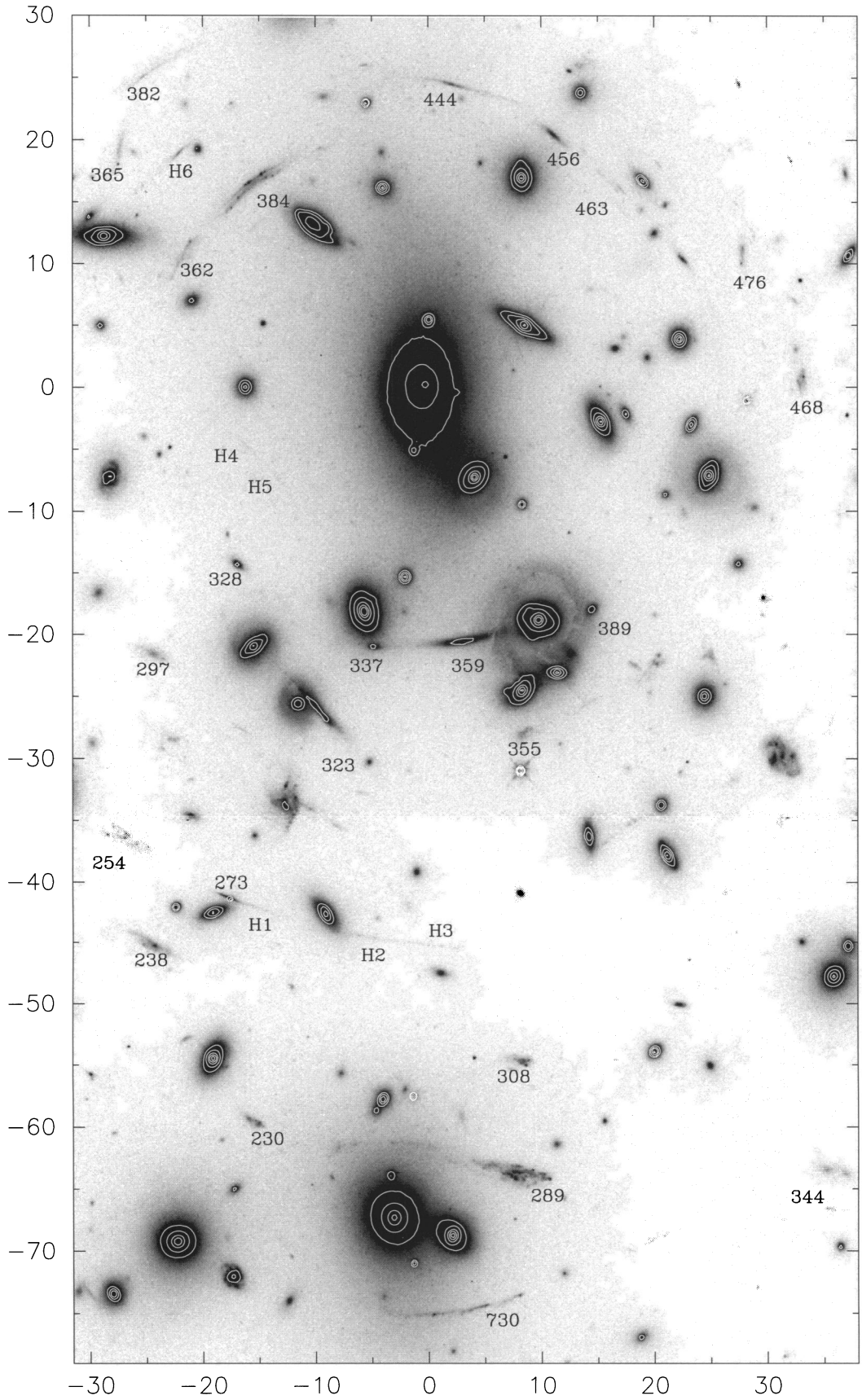

FIG. 1*b*

TABLE 1

CONFIRMED AND CANDIDATE MULTIPLE IMAGES

Multiple Images	R (F702W)	$B - r^a$	μ_{mean}	z
384/468	21.2/22.6	1.0	23.35/23.50	$2.8^{+0.5}_{-0.2}$
359/328/337/389.....	20.3/22.0/21.9/21.5	3.1/3.6/2.6/2.5	22.65/22.65/22.70/22.80	0.702
289	20.5	0.75	23.10	1.034
730	22.9/22.8/23.8 (21.9)	1.43	23.90/23.70/23.45	1.1 ± 0.3
H1–3	~25.5	...	~24.2	1.0 ± 0.3
H4–5	~26.0	...	~24.5	1.6 ± 0.3
444/H6	22.7/23.6	0.35/...	23.85/23.70	1.1 ± 0.1

[a] From Le Borgne et al. 1992 when available; typical errors for red objects can be as high as 0.5 mag (Kneib et al. 1995).

merger of two images of reversed parity. This enables the location of the critical line to be accurately identified. The knots, which presumably represent H II regions in a blue star-forming galaxy, can also be seen in the counterimage No. 468. A further feature of interest is the train-track–like morphology of the source, also replicated in No. 468.

Nos. 359, 328, 337, and 389.—The red arc 359 has a spectroscopic redshift of $z = 0.702$ and shows no internal structure; this is consistent with its identification as a background spheroidal galaxy. It was naturally interpreted as a fold arc, i.e., two merging images (Kneib et al. 1995) with a single counterimage, No. 328. The absence of a strong discontinuity (even in the *HST* image) in the surface brightness along the No. 359 arc can be explained if the surface brightness peak lies just outside (or on) the caustic on the source plane. However, a detailed inspection of the *HST* image demonstrates that this simple picture is unlikely to be correct, as a faint extension of No. 359 is now revealed, which merges with No. 337. From the ground-based data, it was noted that Nos. 337 and 389 had similar colors to No. 359, but no simple model was able to explain such a configuration. If No. 337 is indeed a counterimage of arc 359, then we may consider whether No. 389 is also a counterimage. In § 3, we will show that, by incorporating individual cluster galaxies in the mass model, it is straightforward to show that No. 359 is a fold arc with Nos. 328, 337, and 389 each as counterimages.

No. 289.—In contrast to No. 359, the blue arc 289, with a spectroscopic redshift of $z = 1.034$, exhibits a large amount of internal structure. The arc is luminous and therefore probably highly magnified, but the bright southern end does not appear particularly strongly sheared and is apparently not multiply imaged. This is not too surprising, as one would expect to have, in a complex mass distribution, areas of the image plane with high magnification and small distortion, as is the case for this object. Close inspection of the northern section of this arc indicates that it extends across the halo of the cluster galaxy 244, which is also visible in ground-based data when looking at a true-color image (R. Pelló 1995, private communication). We find that the complex morphology can be explained via a background galaxy straddling the caustic. The majority of the source lies outside the caustic, producing a single, highly magnified, weakly sheared image. The portion within the caustic is multiply imaged and produces the highly elongated tail across the halo of No. 244, forming a long arc made of three different images. Unfortunately, only spectroscopy of the very faint northern section can verify this hypothesis.

A detailed examination of the *HST* image reveals several new potentially important multiply imaged systems:

No. 730.—This very faint thin arc was suggested as a possible lensed feature in the ground-based data but is clearly verified as such by *HST* (although it is still not resolved). The faintness makes it difficult to identify the individual subcomponents at this stage, although a number of bright knots are visible. Nevertheless, the structure suggests a likely cusp arc, as three components can be distinguished. This arc is very different in morphology and color (Table 1) than the No. 289 arc and its extension across No. 244; they must therefore come from a different source, excluding the recent model proposed by Saraniti, Petrosian, & Lynds (1996).

H1–3, H4–5.—These are two impressive multiply imaged systems that were unrecognized in the ground-based studies (Fig. 1*b*). From the morphologies and positions, H1–3 appear to be three images of a section of the disk of No. 273, the remainder of the source being only singly imaged. The very faint features H4–5 ($R \approx 26$) are believed to represent a new, very faint, multiply imaged pair. Several candidates for the counterimage to this pair exist on the opposite side of the cluster.

No. 444 + H6.—No. 444 is a fold arc (two merging images) with H6 as a counterimage.

In summary, the *HST* image not only allows us to confirm the lensed features that underpin the ground-based mass model but also provides additional information that enables us to refine the model. We have identified a total of seven multiply imaged sources seen through the core of Abell 2218. This is a substantial improvement over the ground-based tally and significantly more than the number known in any other cluster at this time. By analyzing these features, we can thus hope for the most detailed view of the mass distribution within a cluster thus obtained. The model refinements derived from these new multiply imaged features are principally in the detailed form of the mass model and lead to little change in the global cluster mass-to-light ratio. However, they can have an effect on the lensing inversion, and we will explore this further in § 5.

2.4. *Arclets and Shear*

Using our previously defined catalog of faint sources (§ 2.2), we now construct a "shear (or deformation) map" defined as the local average of the deformation vector (see § 4) of the lensed galaxies:

$$\langle \bar{\tau} \rangle (x, y) = \iint \bar{\tau}_I(x', y') \omega(x - x', y - y') dx' dy' , \quad (1)$$

where $\omega(x, y)$ is a normalized weighting function. The weighting function chosen was a Gaussian of 20″ FWHM. Figure 3 shows the deformation map within the field of the

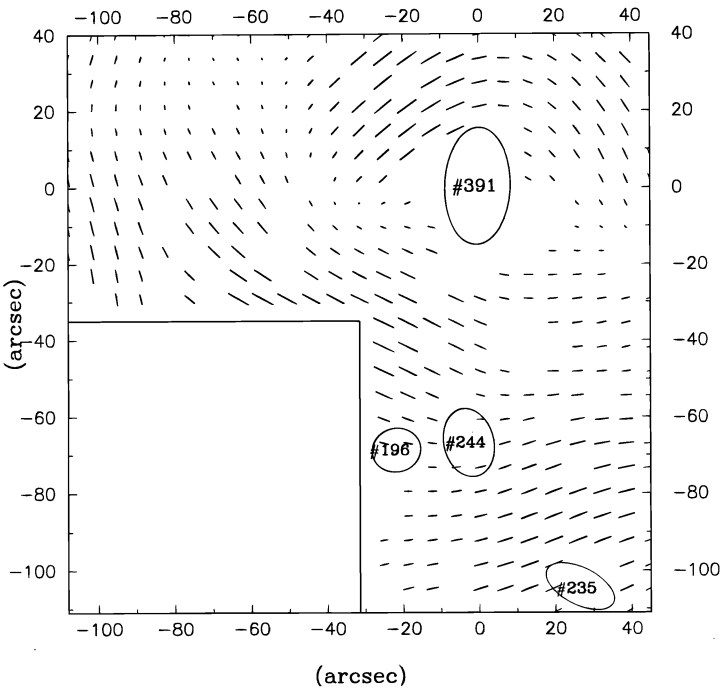

FIG. 3.—Shear map for the cluster center derived from the orientations and ellipticities of the *HST* arclets. The most significant mass components are indicated. The new mass model extends that of Kneib et al. (1995) by including major mass components associated with galaxies 196 and 235 (see Table 3) as well as smaller halos around 30 luminous cluster members (see text for details). At the cluster redshift, 1″ is equivalent to 3.83 kpc.

WFC, upon which we have superposed the location of some of the most luminous cluster members. This map provides a view of the cluster potential with a resolution of 20″ (~75 kpc), allowing us to detect any substructure in the cluster mass distribution on scales larger than the resolution. We now use this information to assist in the construction of a refined model for Abell 2218, taking into account the new details on the multiple images discussed in § 2.3.

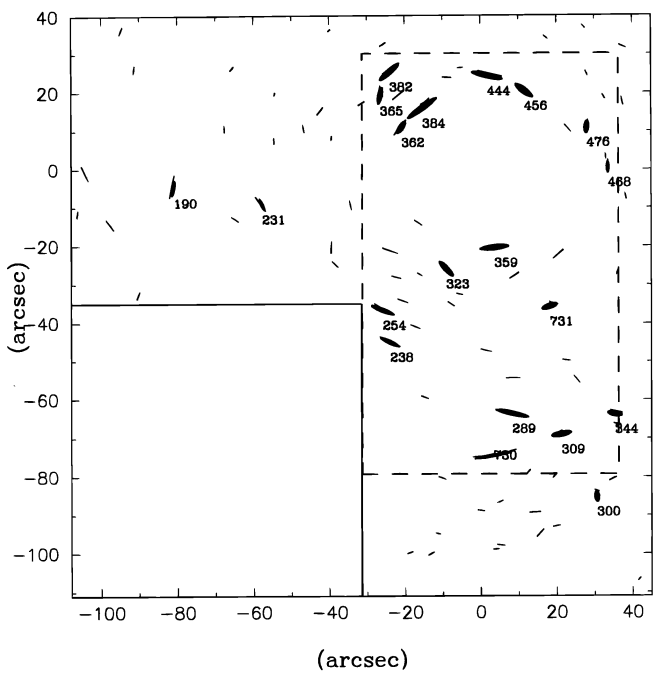

FIG. 4.—Distribution of ~120 arclet candidates with $22 < R < 26$ selected from the *HST* image (*thin lines*) compared to those in the ground-based analysis of Pelló et al. (1992) (*thick lines*). The shear field based on the *HST* sample illustrates the need for further mass components associated with the brighter cluster galaxies.

It is important to recognize that this map differs from the true deformation for a number of reasons, including contamination by foreground and cluster galaxies and also the dependency of the strength of the image deformation on redshift. The former effect has already been minimized by removing the brightest galaxies from our list. Furthermore, we can assume that the bulk of the contaminating galaxies are randomly orientated and thus only dilute the modulus of the shear without affecting its orientation. The earlier ground-based mass model was bimodal in form and centered on the cD galaxy (No. 391) and No. 244. The shear map in these regions suggests, by a higher value of the shear and a change in orientation, that contributions from Nos. 196 and 235 should now be included.

Although the shear map is statistical in nature, the *HST* resolution has encouraged us to define a visually selected sample of the brighter and larger arclets, intermediate to the bright arcs reviewed in the previous section. These sources are sheared sufficiently that their identification as lensed features is more likely, and furthermore, most of them are within spectroscopic reach. Their properties are summarized in Table 2, and Figure 4 compares their distribution with the 20 "arclets" identified from ground-based data (Pelló et al. 1992). The total number of *HST* arclets is now significantly increased. Furthermore, the *HST* data suggest that as many as a third of the ground-based arclets are close galaxy pairs or misidentified edge-on disk galaxies. As we will see below, the multiply imaged pairs represent a particularly tight constraint on the mass distribution.

In summary, the improved resolution of the repaired *HST* allows considerable progress to be made in the identification and understanding of lensed features in Abell 2218. The resolution of the brighter arcs confirms several of the multiply imaged features suggested from the ground-based studies. In particular, the fold arc No. 359 is now identified as a five-image configuration, and a number of new multiply imaged candidates are revealed. Similarly, the *HST* image allows us to identify weakly lensed features (arclets) with greater reliability, both on an individual basis and statistically. In both respects, we are better placed to refine the mass model developed on the basis of ground-based imaging and to identify arclets for redshift determination.

3. MASS MODELING

The mass modeling method we use is based on the precepts developed by Kneib (1993), which have now been successfully applied to describe many different cluster lenses, including MS 2137 (Mellier et al. 1993), A370 (Kneib et al. 1993), Cl 2236 (Kneib, Melnick, & Gopal-Krishna 1994b), Abell 2218 (Kneib et al. 1995), and Cl 0024 (Smail et al. 1996).

The basic approach is to use multiply imaged systems and the mean orientation of the arclets to constrain an analytical representation of the total mass based upon components associated with likely centers of mass, i.e., massive cluster galaxies. Each component is described by a minimal set of parameters: position, ellipticity, orientation, core size, and central velocity dispersion. The associated mass distribution should be approximately isothermal if the central mass is relaxed. The particular analytical expression used is based on the pseudo–isothermal elliptical mass distribution

TABLE 2

CATALOG OF CANDIDATE ARCLETS

ID	R_{cor}	μ_R	z_{photo}	$z-$	z_{opt}	$z+$	Comments
190[a,b]	22.1	23.4	0.1–0.7	...	...	...	Disk galaxy
231[a]	22.2	23.1	0.2–0.7	0.3	0.4	0.6	Compact + disk galaxies[c]
238	23.9	23.5	2.0–3.0	0.8	1.2	1.6	Disk galaxy
254	24.1	23.9	0.2–0.7	0.4	0.6	0.7	
289	22.3	23.1	...	...	1.034	...	
300[a]	24.5	23.6	0.8–2.5	...	...	...	Two compact galaxies
309	25.2	24.0	1.4–2.0	2.5	3.2	4.0	
323[b]	21.1	22.6	1.4–1.6	0.2	0.4	0.6	
344	22.9	23.8	1.8–3.0	...	...	...	Two extended galaxies
359	24.9	22.7	...	...	0.702	...	
362	25.8	24.0	1.8–3.0	0.5	1.1	2.0	
365[b]	23.7	23.8	2.4–3.0	0.3	0.3	0.4	
382	25.7	24.0	1.4–2.6	2.5	3.0	4.0	
384	24.6	23.3	2.6–3.5	2.6	2.8	3.3	
444	25.4	23.5	1.8–3.0	1.0	1.1	1.2	
456	24.5	23.4	0.1–0.7	0.4	0.6	0.8	
467	21.7	22.1	1.2–2.6	0.4	0.4	0.5	
468	23.6	23.5	1.8–3.0	2.6	2.8	3.3	Counterimage of 384
730	25.1	23.7	2.9–3.3	1.0	1.1	1.2	
731	26.0	23.9	2.3–3.1	0.8	1.1	1.4	
273	23.8	22.2	...	0.5	0.6	0.7	
H1–3	~27	~24.2	...	0.7	1.0	1.3	Cusp arc; disk of 273?
H4–5	~27.5	~24.5	...	1.3	1.6	1.9	Fold arc
328	24.9	22.6	...	...	0.702	...	Counterimage of 359
337	24.9	22.7	...	...	0.702	...	Counterimage of 359
389	24.9	22.8	...	...	0.702	...	Counterimage of 359
200	24.9	23.2	...	0.8	1.0	1.3	
229	24.8	23.8	...	0.8	1.0	1.2	
230	24.1	23.3	...	0.3	0.3	0.4	
236	23.0	23.3	...	0.4	0.4	0.5	
297	23.8	23.7	...	0.5	0.6	0.7	
308	23.4	23.4	...	0.5	0.6	0.8	
355	23.8	23.7	...	0.3	0.4	0.6	
408	22.2	22.7	...	0.2	0.4	0.8	
464	24.8	23.3	...	0.9	1.1	1.3	

NOTE.—The catalog of candidate arclets from our *HST* WFPC2 image. Objects with z_{photo} represent candidate arclets from Pelló et al. (1992) that lie within the *HST* WFPC2 field.

[a] Misidentification (edge-on galaxy or a close pair).

[b] Suspected not to be strongly lensed when comparison is made with the shear orientation.

[c] Values are given for the disk galaxy.

(PIEMD) with ellipticity $e = (a - b)/(a + b)$ derived by Kassiola & Kovner (1993):

$$\Sigma(x, y) = \Sigma_0 \frac{r_c}{\sqrt{r_c^2 + \rho^2}} = \frac{\sigma_0^2}{2G\sqrt{r_c^2 + \rho^2}}, \quad (2)$$

with

$$\rho^2 = \frac{x^2}{(1 + e)^2} + \frac{y^2}{(1 - e)^2}. \quad (3)$$

This expression has the advantage of describing mass distributions with arbitrarily large ellipticities. For each component used, we smoothly truncate the elliptical mass distributions (cf. appendix of Kassiola & Kovner 1993), using a linear combination of two PIEMD components:

$$\Sigma(x, y) = \Sigma_0 \frac{r_c r_{cut}}{r_{cut} - r_c} \left(\frac{1}{\sqrt{r_c^2 + \rho^2}} - \frac{1}{\sqrt{r_{cut}^2 + \rho^2}} \right), \quad (4)$$

where r_{cut} is the truncation radius (the surface mass density falls as r^{-3} for $r \gg r_{cut}$). The total mass of such a truncated mass distribution is finite, and for $r \gg r_{cut}$ in the limit $e \to 0$,

$$M_{tot} = 2\pi\Sigma_0 r_c r_{cut} = \frac{\pi}{G} \sigma_0^2 r_{cut}^2. \quad (5)$$

The ground-based mass model for Abell 2218 (Kneib et al. 1995) was based on two major components associated with galaxies 391 and 244. As discussed in § 2.3, the detailed information now available from the multiple images (particularly No. 359 and its counterimages), and, to a lesser extent, some of the fine structure visible in the shear map (Fig. 3), encourages us to improve on this model by incorporating the effect of halos associated with components around Nos. 235 and 196 and other individual cluster galaxies. For each component, the center, ellipticity, and orientation are matched to those observed for the associated light distribution (as is the case for those associated with Nos. 391 and 244). However, the dynamical parameters r_c, r_{cut}, and σ_0 for these four main components are kept as free parameters.

When including galaxy-scale components into our model, it is clear that such a refinement could, in principle, be continued indefinitely. In practice, we included all galaxies with $R < 19.5$ (as the magnitude increases, the mass of each galaxy becomes small, and their lensing effects become negligible). In total, we incorporate halos associated with 30 luminous cluster galaxies into the mass model. For each halo, the ellipticity and orientation match those observed for the galaxy light distribution. The other mass parameters are scaled according to the galaxy luminosity following

Brainerd, Blandford, & Smail (1996):

$$\sigma_0 = \sigma^*(L/L^*)^{1/4} , \quad (6)$$

$$r_{\rm cut} = r^*_{\rm cut}(L/L^*)^{1/2} , \quad (7)$$

where σ^* and $r^*_{\rm cut}$ are free parameters in the minimization procedure. Furthermore, to have a profile that is identical from one galaxy to another, we scale the core radius r_0 in the same way as $r_{\rm cut}$:

$$r_0 = r^*_0(L/L^*)^{1/2} . \quad (8)$$

The mass of individual galaxies scales as the luminosity, with

$$M_{\rm tot} = \frac{\pi}{G}(\sigma^*)^2 r^*_{\rm cut}\left(\frac{L}{L^*}\right) . \quad (9)$$

This simple scaling was chosen because it is physically motivated, it conserves the M/L-ratio of galaxies, and it has only three parameters, namely, σ^*, $r^*_{\rm cut}$, and r^*_0. However, with better data, we should be able to improve such simple scaling laws.

It is worth emphasizing that, by themselves, the individual galaxy halos do not contain enough mass to reproduce all the lensed features observed in the cluster. In other words, we must retain cluster-scale mass components associated with the brighter cluster galaxies (the central cD galaxy [No. 391] and Nos. 235, 196, and 244).

To constrain the composite mass model, we first define a χ^2-estimator as the quadratic sum of the differences between the source parameters (position, orientation, and ellipticity) for each set of multiple images (see Table 1), plus the observed shear as represented by the quadratic sum of $\tau_{\rm pot}\langle\tau_I\rangle \sin 2(\theta_{\rm pot} - \langle\theta_I\rangle)$. We then minimize this estimator by varying the parameters of the mass model. As indicated above, the greatest constraints come from the multiple images. To stabilize and speed up the convergence, we specify the location of the infinite magnification point in the fold or cusp images (i.e., the location of the symmetry break in the case of No. 384 or the luminosity peak of No. 359 and the saddle between Nos. 359 and 337 in the case of arc 359 at $z = 0.702$).

The best fiducial model resulting from the *HST* data is presented in Table 3. A contour plot of the mass distribution is shown in Figure 5, where the shear field is also shown for a source plane at $z_S = 1$. Although small discrepancies remain between this predicted shear map and that observed, it must be remembered that the observed shear is relatively poorly defined, given the limited arclet sample and various "edge effects." We return to the question of the possible *uniqueness* of this mass model later. At this point we simply note that the mass model is consistent with the very detailed constraints provided by the multiple images recognized by *HST*.

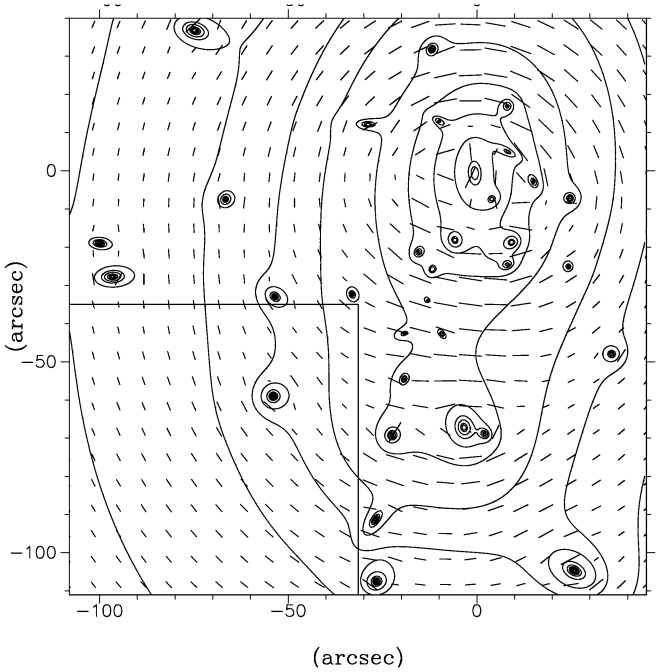

FIG. 5.—Contour map for the adopted mass distribution and the shear map implied for a source plane at $z_S = 1$. Contours correspond from the lowest to the highest to a density of 0.5, 1, 1.5, 2, 3, 4, 5, 6, 8, and 10×10^9 $M_\odot$ kpc^{-2}. At the cluster redshift, 1″ is equivalent to 3.83 kpc.

Although the difference between the *HST* and ground-based mass models is small when considering global properties such as cluster mass-to-light ratio, we show in § 5 that there can be variations in the lensing inversion for specific arclets, depending upon their location. The principle change is in the detailed granularity of the mass distribution, leading to a more precise inversion.

4. GRAVITATIONAL LENSING FORMALISM

We now turn to the primary purpose of the paper, namely, to take our well-constrained mass model for Abell 2218 and use it to derive statistical redshift distributions for the large sample of faint arclets discussed in § 2.4. In what follows, we extend the original discussion of Kneib et al.

TABLE 3

FIDUCIAL PARAMETERS OF MASS MODEL

Cluster-Size Component	x_c (arcsec)	y_c (arcsec)	a/b	θ (deg)	r_c (kpc)	σ (km s^{-1})	$r_{\rm cut}$ (kpc)
No. 391.....	0.0	0.0	1.37	−10	76	1335	710
No. 244.....	−3.0	−67.0	1.26	111	33	495	450
No. 196.....	−22.0	−69.0	1.05	56	50	470	270
No. 235.....	26.0	−104.5	1.22	152	30	306	200

Galaxy-Size Component	r_c (kpc)	σ (km s^{-1})	$r_{\rm cut}$ (kpc)	$M_{\rm tot}$ (10^{12} $M_\odot$)	M/L_V ($M_\odot/L_\odot$)
For $M^*_V = -23$.....	1.0	245.0	30	1.3	9

NOTES.—Fiducial parameters of the various components in the improved mass model of Abell 2218. Positions and orientations are defined on the WFPC2 image (Fig. 1*a*), with the position angle θ increasing counterclockwise from the x-axis.

(1994a), developing a formalism for estimating the errors in the inversion redshifts of individual galaxies. This will be particularly useful, as we have a range of lensed features from relatively bright arclets, many of which can be recognized as lensed on an individual basis, to fainter images, which can only be treated statistically.

4.1. *General Equations*

The gravitational lensing formalism we use is based on the original treatise presented by Kneib et al. (1994a). The lens mapping is described by the transformation

$$\boldsymbol{u}_S = \boldsymbol{u}_I - \mathscr{D}\nabla\phi(\boldsymbol{u}_I)\,, \tag{10}$$

where $\boldsymbol{u}_S$ is the position of the source, $\boldsymbol{u}_I$ is the position of the image, $\mathscr{D}$ is the dimensionless ratio $D_{\rm LS}/D_{\rm OS}$, and ϕ is the projected Newtonian potential normalized by $2/c^2$.

A distant galaxy can be described to the first order by five geometrical parameters: its centroid (x_c, y_c), complex deformation $\bar{\tau} = \tau e^{2i\theta}$, and size s.

The first moment of the weighed surface brightness $\mu(x, y)$ distribution gives the position of the centroid (x_c, y_c):

$$x_c = \frac{1}{\mu_W}\iint W(x, y)\mu(x, y)x\,dx\,dy\,,$$
$$y_c = \frac{1}{\mu_W}\iint W(x, y)\mu(x, y)y\,dx\,dy\,, \tag{11}$$

with

$$\mu_W = \iint W(x, y)\mu(x, y)dx\,dy\,. \tag{12}$$

The weighting function $W(x, y)$ can be adjusted to minimize the error in the determination of the centroid.

The second-order moment matrix $\mathbf{M}$ gives the shape of the galaxy ($\bar{\tau} = \tau e^{2i\theta}$), i.e., its equivalent ellipse of major axis a, minor axis b, and orientation θ:

$$\mathbf{M} = \frac{1}{\mu_W}\iint W(x, y)\mu(x, y)x_i x_j\,dx\,dy$$
$$= \begin{pmatrix} M_{xx} & M_{xy} \\ M_{xy} & M_{yy}\end{pmatrix} \propto \mathbf{R}_\theta \begin{pmatrix} a^2 & 0 \\ 0 & b^2\end{pmatrix}\mathbf{R}_{-\theta}\,, \tag{13}$$

where $\mathbf{R}_\theta$ is the rotation matrix of angle θ. Note that different weighting functions can be chosen in computing the first- and second-moment integrals, depending upon which is required with higher accuracy. The weighting factor is more critical in dealing with ground-based data than with *HST* images because of the effects of seeing (Bonnet & Mellier 1995; Kaiser, Squires, & Broadhurst 1995; Wilson, Cole, & Frenk 1996). In our analysis, we used the simple weighting function

$$W(x, y) = \begin{cases} 1\,, & \text{if } \mu < \mu_{\rm ISO}\,, \\ 0\,, & \text{if } \mu > \mu_{\rm ISO}\,. \end{cases} \tag{14}$$

The size parameter (s) is defined as

$$s = 2\sqrt{\det \mathbf{M}} \propto 2ab\,, \tag{15}$$

and the deformation matrix $\mathbf{D}$ is

$$\mathbf{D} = \frac{\mathbf{M}}{2\sqrt{\det \mathbf{M}}} = \begin{pmatrix} \delta + \tau_x & \tau_y \\ \tau_y & \delta - \tau_x\end{pmatrix}, \tag{16}$$

where $\bar{\tau} = \tau_x + i\tau_y = \tau e^{2i\theta}$ is the complex deformation and $\delta = (1 + \tau^2)^{1/2}$ is the real distortion parameter. In terms of the major and minor axes, these are

$$\tau = \frac{a^2 - b^2}{2ab}\,, \quad \delta = \frac{a^2 + b^2}{2ab}\,. \tag{17}$$

Further, the complex shear $\bar{g}$ and the complex ellipticity $\bar{\varepsilon}$ are defined as

$$\delta = 1 + \bar{g}\bar{\tau}^*\,, \quad g = \frac{a - b}{a + b}\,, \tag{18}$$

$$\bar{\varepsilon} = \frac{\bar{\tau}}{\delta}\,, \quad \varepsilon = \frac{a^2 - b^2}{a^2 + b^2}\,, \tag{19}$$

where an asterisk denotes the conjugate of a complex number. The lensing equation for the moment matrix is given by

$$\mathbf{M}_S = \mathbf{a}^{-1}\mathbf{M}_I{}^t\mathbf{a}^{-1} \tag{20}$$

(Kochanek 1990), where subscript S refers to the source, I to the image, and $\mathbf{a}^{-1}$ is the inverse of the amplification matrix, defined as the Hessian of the lens mapping (eq. [10]):

$$\mathbf{a}^{-1} = \begin{pmatrix} \mathscr{D}\partial_{xx}\phi & -\mathscr{D}\partial_{xy}\phi \\ -\mathscr{D}\partial_{xy}\phi & 1 - \mathscr{D}\partial_{yy}\phi\end{pmatrix}$$
$$\equiv \begin{pmatrix} 1 - \kappa + \gamma_x & \gamma_y \\ \gamma_y & 1 - \kappa - \gamma_x\end{pmatrix}, \tag{21}$$

where κ and $\bar{\gamma} = \gamma_x + i\gamma_y = \gamma e^{2i\theta_{\rm pot}}$ are the usual convergence and shear parameters. We denote $\gamma = \mathscr{D}\tilde{\gamma}$ and $\kappa = \mathscr{D}\tilde{\kappa}$ to separate the distance and mass effects. Here $\theta_{\rm pot}$ is the direction of the shear (independent of the redshift of the source) and is defined by

$$\tan 2\theta_{\rm pot} = \frac{2\partial_{xy}\phi}{\partial_{xx}\phi - \partial_{yy}\phi}\,. \tag{22}$$

Equivalently, for the potential we can define the parameters $\bar{g}_{\rm pot}$, $\bar{\tau}_{\rm pot}$, and $\delta_{\rm pot}$:

$$\bar{g}_{\rm pot} = \frac{\bar{\gamma}}{1 - \kappa}\,, \quad \tau_{\rm pot} = \frac{2\bar{g}_{\rm pot}}{1 - \bar{g}_{\rm pot}\bar{g}^*_{\rm pot}}\,, \quad \delta = 1 + \bar{g}_{\rm pot}\bar{\tau}^*_{\rm pot}\,. \tag{23}$$

For a circular source using this notation, the lens transformation yields $g_I = g_{\rm pot}$, $\tau_I = \tau_{\rm pot}$, etc.

The determinant of equation (20) yields the lensing transformation of the object's size:

$$s_S = |\det \mathbf{a}^{-1}|\, s_I\,. \tag{24}$$

Dividing equation (20) by equation (24), we have the lens equation for the deformation matrix:

$$D_S = \frac{1}{|\det \mathbf{a}^{-1}|}\,\mathbf{a}^{-1}D_I{}^t\mathbf{a}^{-1}\,. \tag{25}$$

From equation (25), the lens equation for the complex deformation $\bar{\tau}_S$ is also derived:

$$\text{sgn}\,(\det \mathbf{a}^{-1})\bar{\tau}_S = \bar{\tau}_I - \bar{\tau}_{\rm pot}[\delta_I - \tau_I\,\text{Re}\,(\bar{g}_I\bar{g}^*_{\rm pot})]\,. \tag{26}$$

The inverse equation is found by exchanging the subscripts I and S and the signs of $\bar{\tau}_{\rm pot}$ and $\bar{g}^*_{\rm pot}$. This yields

$$\text{sgn}\,(\det \mathbf{a}^{-1})\bar{\tau}_I = \bar{\tau}_S + \bar{\tau}_{\rm pot}[\delta_S + \tau_S\,\text{Re}\,(\bar{g}_S\bar{g}^*_{\rm pot})]\,. \tag{27}$$

A vectorial representation of equation (27) is shown in Figure 6. *The complex deformation of the image is just the*

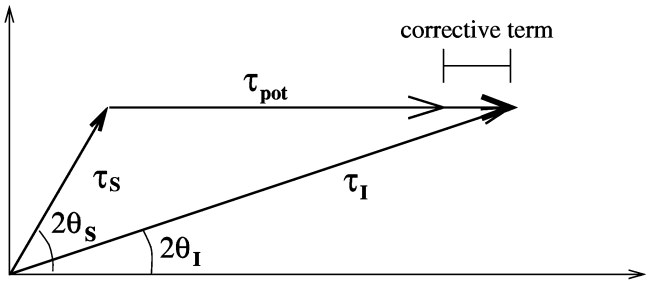

FIG. 6.—Lens deformation diagram (see text for definition of quantities).

vector sum of the intrinsic source shape and the induced deformation from the potential, corrected in the strong-lensing regime by a factor $\delta_S + \tau_S \, \mathrm{Re}\,(\bar{g}_S \bar{g}^*_{pot})$. In the weak-shear regime ($\det \mathbf{a}^{-1} > 0$), the correction tends to unity, and equation (27) becomes

$$\bar{\tau}_I = \bar{\tau}_S + \bar{\tau}_{pot} \, . \tag{28}$$

Using the local shear axes, equation (26) reads

$$\mathrm{sgn}\,(\det \mathbf{a}^{-1})\tau_{S,x} = \delta_{pot}\,\tau_{I,x} - \tau_{pot}\,\delta_I = \delta_{pot}\,\delta_I(\varepsilon_I - \varepsilon_{pot}) \, , \tag{29}$$

$$\mathrm{sgn}\,(\det \mathbf{a}^{-1})\tau_{S,y} = \tau_{I,y} \, . \tag{30}$$

Note that $|\tau_y|$ is a conserved quantity under the lens transformation.

4.2. *Distribution in Ellipticity and Redshift*

The source ellipticity distribution can be estimated from deep *HST* images of fields outside rich clusters. A large sample of suitable fields is available in the Medium Deep Survey archive (Griffiths et al. 1994). Analysis of these (Ebbels, Kneib, & Ellis 1996) reveals that the observed distribution of image shapes for brighter galaxies is well fitted by the functional form

$$p(\tau_{S,x}, \tau_{S,y}) \propto \exp\left[-\left(\frac{\tau_{S,x}^2 + \tau_{S,y}^2}{\sigma_\tau^2}\right)^\alpha\right] \tag{31}$$

with $\alpha \sim 1.15$ and $\sigma_\tau \sim 0.33$. This distribution has a maximum at $(\tau_x, \tau_y) = (0, 0)$ and is also radially symmetric (because of the random orientations of unlensed field galaxies). We stress however that the form of this distribution does depend strongly upon the sizes of the galaxies and their magnitudes (Ebbels et al. 1996).

Since $|\tau_y|$ is conserved by lensing, *in the frame of the local shear*, we have the conditional probabilities

$$p(\tau_{S,x}, \tau_{S,y}) = p(\tau_{S,x}, \tau_{I,y}) = p[\delta_{pot}(z_S)\tau_{I,x} - \tau_{pot}(z_S)\delta_I, \tau_{I,y}] = p(z\,|\,I, \mathrm{mass})\,p_{\tau_{S,y}}(\tau_{S,y}) \, . \tag{32}$$

In other words, the conditional redshift probability (given the image shape *and* the mass model) is simply the source shape probability divided by that of $\tau_{S,y}$. From equation (31),

$$p(z\,|\,I, \mathrm{mass}) = \frac{p(\tau_{S,x}, \tau_{S,y})}{p_{\tau_{S,y}}(\tau_{S,y})} = \frac{1}{\sqrt{2\pi}\,\sigma_\tau^2} \exp\left\{-\frac{[\delta_{pot}(z_S)\tau_{I,x} - \tau_{pot}(z_S)\delta_I]^2}{2\sigma_\tau^2}\right\}, \tag{33}$$

which reproduces the intuitive prescription of Kneib et al. (1994a) that the maximum of the redshift probability function for a given image corresponds to the minimum deformation of the source.

When the image is outside the critical line, τ_{pot} is an increasing function of redshift—with positive $\tau_{I,x}$ if the orientation is within 45° of the shear direction, and negative otherwise. If $\tau_{I,x}$ is positive but not too large, $p(z\,|\,I, \mathrm{mass})$ has a maximum for $\varepsilon_{I,x} = \varepsilon_{pot}(z_S)$, and the most probable redshift is finite. However, when $\tau_{I,x}$ is too large, $p(z\,|\,I, \mathrm{mass})$ is an increasing function of redshift, leading to a most probable redshift $z = \infty$. If $\tau_{I,x}$ is negative, then $p(z\,|\,I, \mathrm{mass})$ is a decreasing function of redshift, yielding a most probable redshift $z = z_{lens}$ (see Fig. 7). In the latter two cases, no "sensible" estimate of the redshift of the galaxy can be derived.

4.3. *Uncertainties in the Redshift Determination*

We now discuss the uncertainties that arise when determining faint galaxy redshifts with a gravitational telescope. There are three sources of error: those arising from image shape (errors in the deformation $\bar{\tau}_I$), the lens mass model (errors in κ, γ, and θ_{pot}), and statistical errors introduced by the contamination of the arclet sample by foreground or cluster galaxies. The first two errors are concerned with individual arclets while the third affects the properties of the sample as a whole.

4.3.1. *Individual Errors*

We begin by considering the relative error in z. Differentiating $g_{pot} = \mathscr{D}\tilde{\gamma}/(1 - \mathscr{D}\tilde{\kappa})$, we have

$$\frac{(z - z_L)\mathscr{D}'}{\mathscr{D}}\frac{dz}{z - z_L} = \frac{d\mathscr{D}}{\mathscr{D}} = (1 - \mathscr{D}\tilde{\kappa})\frac{dg_{pot}}{g_{pot}} - (1 - \mathscr{D}\tilde{\kappa})\frac{d\tilde{\gamma}}{\tilde{\gamma}} - \mathscr{D}d\tilde{\kappa} \, . \tag{34}$$

The term $\mathscr{D}/(z - z_L)\mathscr{D}'$ is almost proportional to $(z - z_L)$, indicating that the accuracy of the lensing-inferred redshifts is lower at larger redshift (see Fig. 8).

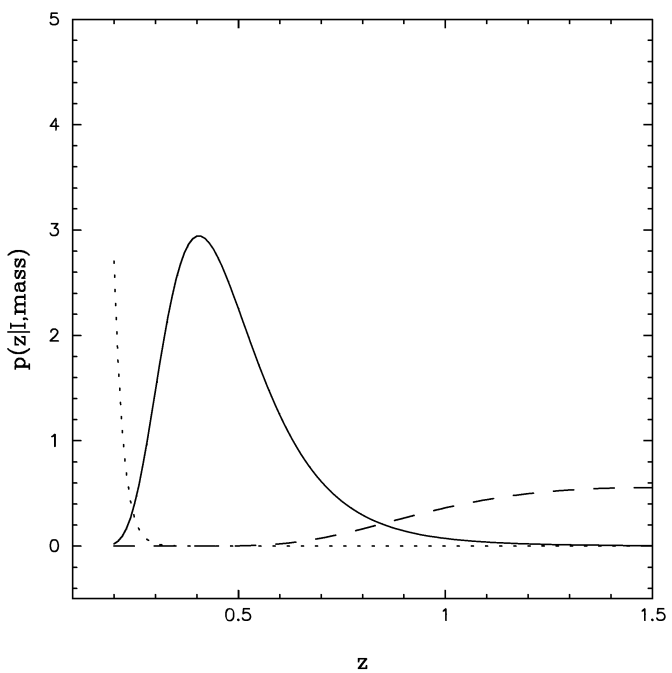

FIG. 7.—Redshift probability distribution for $\tau_{I,x} > 0$ (*solid*, *dashed lines*) and $\tau_{I,x} < 0$ (*dotted line*); see text for details.

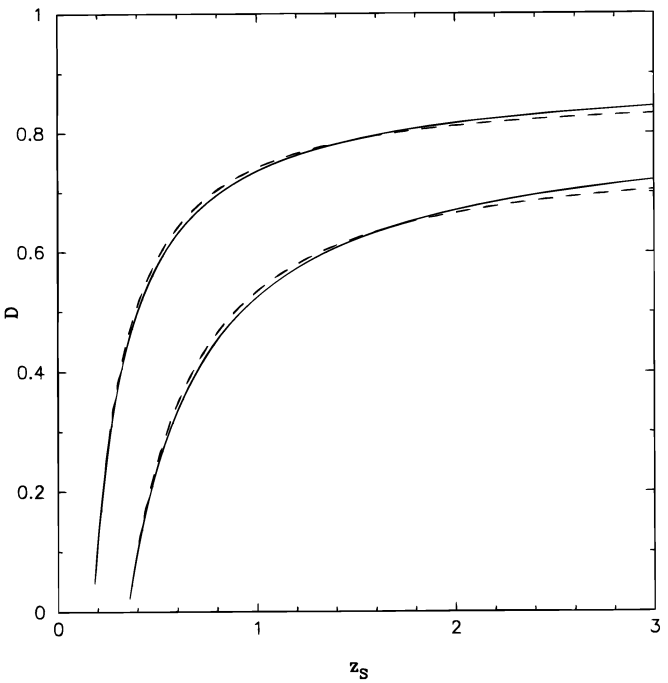

FIG. 8*a*

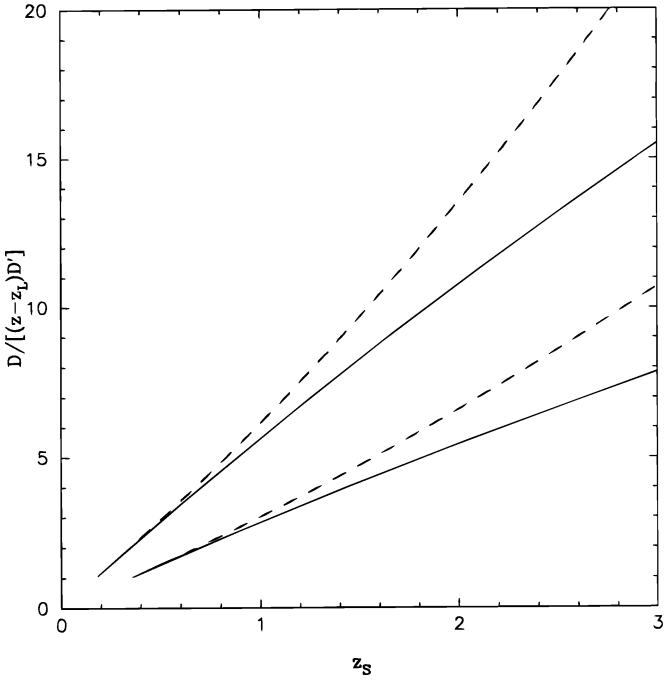

FIG. 8*b*

FIG. 8.—(*a*) $\mathscr{D}$-parameter vs. source redshift for cluster lenses at $z = 0.175$ and $z = 0.35$. The solid line is for $\Omega_0 = 1$, and the dashed line is for $\Omega_0 = 0.2$. (*b*) $\mathscr{D}/[(z - z_L)\mathscr{D}']$ vs. source redshift, illustrating that the higher the source redshift, the greater the uncertainty in the inverted redshift. Note that the redshift of a distant source is more accurately derived by using a high-redshift lens.

Moreover, for the maximum of the redshift probability function,

$$\frac{dg_{\rm pot}}{g_{\rm pot}} = \delta_{\rm pot}\frac{d\varepsilon_{\rm pot}}{\varepsilon_{\rm pot}} = \delta_{\rm pot}\frac{d\varepsilon_{I,x}}{\varepsilon_{I,x}} = \delta_{\rm pot}\left(\frac{d\varepsilon_I}{\varepsilon_I} - 2\tan 2\theta_I\, d\theta_I\right), \tag{35}$$

and thus the total error in the estimate of the most probable redshift is

$$\frac{d\mathscr{D}}{\mathscr{D}} = (1 - \mathscr{D}\tilde{\kappa})\delta_{\rm pot}\left(\frac{d\varepsilon_I}{\varepsilon_I} - 2\tan 2\theta_I\, d\theta_I\right) - (1 - \mathscr{D}\tilde{\kappa})\frac{d\tilde{\gamma}}{\tilde{\gamma}} - \mathscr{D}\, d\tilde{\kappa}\,. \tag{36}$$

We now turn to the likely uncertainties in measured image ellipticities ε_I and position angles θ_I. The former has the following effect:

$$\frac{d\mathscr{D}}{\mathscr{D}} = (1 - \mathscr{D}\tilde{\kappa})\delta_{\rm pot}\frac{d\varepsilon_I}{\varepsilon_I}\,. \tag{37}$$

An overestimate of ε_I leads (in the subcritical part of the lens) to an overestimated redshift. If the image is close to a critical line, then a small error in ε_I produces a large error in z since $\delta_{\rm pot}$ diverges. However, for the bulk of the arclets this is not a problem, as we are not in the multiple-image regions and $(1 - \mathscr{D}\tilde{\kappa})\delta_{\rm pot}$ is in general less than 1 (as $\delta_{\rm pot} \sim 1$ and $1 - \mathscr{D}\tilde{\kappa} < 1$). Our simulations of *HST* images of faint galaxies show that there is a tendency to underestimate the image ellipticity at large ellipticity and overestimate the ellipticity at small ellipticity, although these effects can be statistically corrected. However, for small ellipticities and small objects, it is difficult to determine statistically the true image ellipticity (see § 5).

Errors in the measured orientation θ_I,

$$\frac{d\mathscr{D}}{\mathscr{D}} = -(1 - \mathscr{D}\tilde{\kappa})\delta_{\rm pot}\, 2\tan 2\theta_I\, d\theta_I\,, \tag{38}$$

have the same dependence on $\delta_{\rm pot}$ as the ellipticity. However, as the orientation is usually the best measured characteristic of an image, and because the error is symmetrically distributed, the bias is less serious than for the ellipticities. Nevertheless, when $\theta_I \sim \pi/2$ ($\varepsilon_{I,x} \sim 0$), the errors can become very large.

Finally, the errors in the cluster mass model, in $\tilde{\kappa}$,

$$\frac{d\mathscr{D}}{\mathscr{D}} = -\mathscr{D}\, d\tilde{\kappa} = -\frac{d\Sigma}{\Sigma_{\rm crit}}\,, \tag{39}$$

and the error in $\tilde{\gamma}$,

$$\frac{d\mathscr{D}}{\mathscr{D}} = -(1 - \mathscr{D}\tilde{\kappa})\frac{d\tilde{\gamma}}{\tilde{\gamma}}\,, \tag{40}$$

demonstrate the relationship between the distance estimates and the parameters of the mass model. These relationships indicate that if we adopt an incorrect mass model for the lens, which overestimates the local mass in the lens and hence predicts a too-high value of κ and γ as a function of redshift, when we compare the predicted shear field with the observed one we will tend to underestimate the typical redshift to compensate for the (incorrect) high predicted shear. Such a situation might occur if we ignored some galaxy-size components in the lens model, which can strongly change the intensity and orientation of the deformation near a criti-

cal area of the lens. It is therefore very important to take these components into account.

An advantage of the *Hubble Space Telescope* is the stability of the high-resolution imaging, which minimizes problems that plague ground-based studies of faint object shapes (seeing, tracking, field astigmatism, and their time variability). While *HST*'s capabilities are an order of magnitude better than the ground-based facilities, the limiting factors for accurate measurement of the shapes of faint and compact galaxies now become photon noise and pixel-sampling effects.

A key point in determining reliable redshifts is the *absolute* calibration of the mass model. This is best addressed by using a number of spectroscopically confirmed lensed features in the cluster, while the morphology of the mass can be best determined by using the geometry of any multiply imaged sources present (Mellier et al. 1993; Kneib et al. 1993; Smail et al. 1995b). For spectroscopic arcs, Abell 2218 is one of the best clusters for our purposes since Pelló et al. (1992) have secured accurate redshifts for two of the giant arcs in the cluster core. Similarly, the presence of at least seven multiply imaged sources in Abell 2218, identified by use of *HST*, means that we can strongly constrain not only the absolute mass in the cluster core but also the detailed form of its distribution. We can thus expect that remaining uncertainties in the mass distribution will predominantly arise from unresolved granularity on scales ≤ 75 kpc not attached to any galaxy. The fact that we can make such a statement attests to the detailed view of the cluster mass provided by lensing.

4.3.2. *Sample Selection Contaminations*

The final uncertainty we must consider arises from contamination of the arclet catalog by foreground galaxies and, in particular, cluster members. Indeed, considering only the number of galaxies detected within the WFPC2 field and comparing this to deep field counts (Smail et al. 1995c), ~ 30 galaxies per magnitude are cluster members down to $R \sim 24.5$ (Fig. 2). This contamination is stronger in the center of the cluster than in the outer parts, as the surface density of galaxies within a cluster falls faster than $1/r$.

If the contaminating galaxies are randomly orientated, the mean observed deformation is reduced below the true value, and hence we obtain an artificial reduction of the mean redshift of the background population. In the absence of a reliable distance separation on the basis of arclet colors, we have developed a statistical method to estimate the unlensed contamination.

Lensing displaces the ellipticity distribution of faint sources from that observed for blank fields (or unlensed sources), which should be centered on the null ellipticity; this is illustrated schematically in Figure 9. As discussed in § 4.2, redshifts can only be estimated for images with orientations within 45° of the predicted shear direction (i.e., arclets with $\tau_{I,x} > 0$). Images with $\tau_{I,x} < 0$ must either be cluster members, foreground galaxies, or, conceivably, lensed background objects that are insufficiently deformed to move them into the $\tau_{I,x} > 0$ region. The number of images with $\tau_{I,x} < 0$ therefore provides an upper limit on contamination by unlensed galaxies, and an improved estimate can be determined by considering those lying within the bulk of the ellipticity distribution ($\tau_I < \sigma_\tau$ and $\tau_{I,x} < 0$). By applying a $\pi/2$ rotation prior to inversion, we can also obtain an estimate of the contamination as a function of redshift and directly subtract this spurious $N(z)$ from that derived for the total distribution. Although this only provides a statistical correction for contamination, it gives a good indication of the stability of the derived $N(z)$.

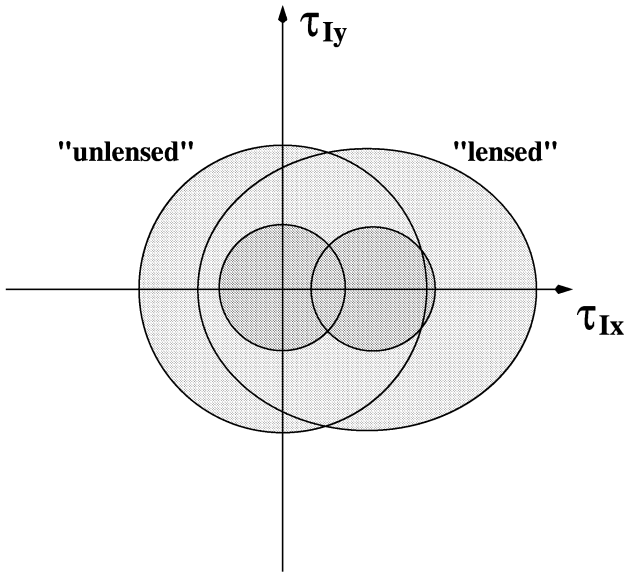

FIG. 9.—Ellipticity distribution showing that observed is the sum of the lensed and unlensed galaxies' vectors.

5. DETERMINING THE FIELD REDSHIFT DISTRIBUTION TO $R \simeq 25.5$

We now use the photometric catalog of faint arclet candidates discussed in § 2, together with the lensing inversion method presented in § 4, to derive the likely redshift distribution $N(z)$ of faint background galaxies viewed through the center of Abell 2218.

In order to quantify the errors in our determination of $N(z)$, we must first estimate uncertainties in the shape measurements of individual arclets as a function of their size and apparent magnitude. This is important in determining the useful limit of our *HST* image for accurate inversion. To accomplish this, we simulated $\sim 300{,}000$ images of different known sizes and ellipticities and then reproduced the detection characteristics applicable to our *HST* image. By comparing the actual galaxy catalog to its simulated equivalent, the dispersion in the realized shape and orientation can be examined as a function of apparent magnitude (Fig. 10). The formalism of § 4 then gives, for each image, the likely redshift error arising from these observational uncertainties.

The simulations are very helpful in revealing two important limitations that apply in deriving redshift distributions from lensing data:

First, we find the redshift error does not track the measured apparent magnitude very well for a realistic distribution of image properties, but depends more closely on the intrinsic shape and signal-to-noise ratio of each image. Clearly the most interesting region for consideration is that which lies beyond the current spectroscopic limit, viz., $R > 23$. In the context of our relatively short *HST* exposure of Abell 2218, Figure 10*d* shows that the uncertainty in the measurement of ellipticities increases significantly beyond $R = 25$ (but strongly depends on the size and the ellipticity of the objects), and thus inversion becomes highly uncer-

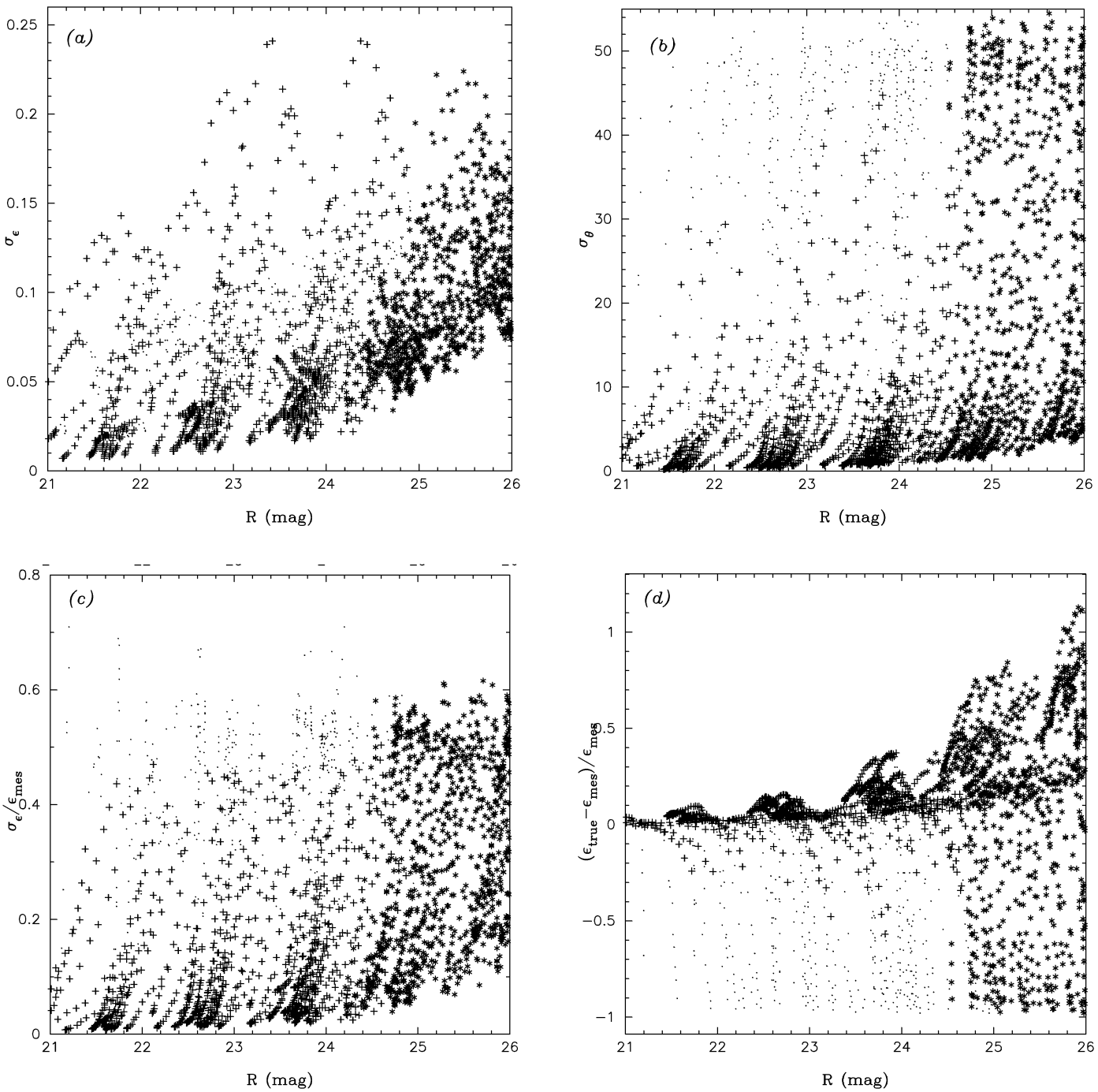

FIG. 10.—Simulated errors for image parameters relevant to lensing inversion as function of apparent magnitude: (*a*) dispersion on the ellipticity σ_ϵ, (*b*) dispersion on the orientation σ_θ, (*c*) relative error $\sigma_\epsilon/\epsilon_{meas}$, and (*d*) relative error $(\epsilon_{true} - \epsilon_{meas})/\epsilon_{meas}$. Each data point was determined from 100 realizations of the same source; dots denote galaxies with small ellipticities ($\epsilon < 0.2$), asterisks denotes galaxies whose isophotal area is less than 50 pixels, and plus signs denote galaxies with intrinsic large ellipticities ($\epsilon > 0.2$) and large isophotal area (> 50 pixels).

tain. Although we can correct for this effect *statistically* (see § 4.3.2, Fig. 11), the uncertainty in this correction clearly could swamp the signal from those sources for which reliable inversion is possible.

Second, even with adequate signal-to-noise ratio for all images, Δz depends on z itself (Fig. 8). A single cluster lens can thus only usefully constrain the number of sources lying in a specific redshift range ($0.5 < z < 1.5$ for Abell 2218), although some information is available on the overall $N(z)$ as well.

The first limitation is more serious, as it emphasizes that those samples for which lensing-induced redshift distributions can be reliably determined are unlikely to be strictly magnitude limited as has been the case traditionally for ground-based spectroscopic surveys. Notwithstanding the contamination from sources that are not amenable to inversion, a magnitude-limited arclet sample would never produce a magnitude-limited source sample, because of the variable magnifications. However, the fact that little can be said about a subset of faint sources is a more serious diffi-

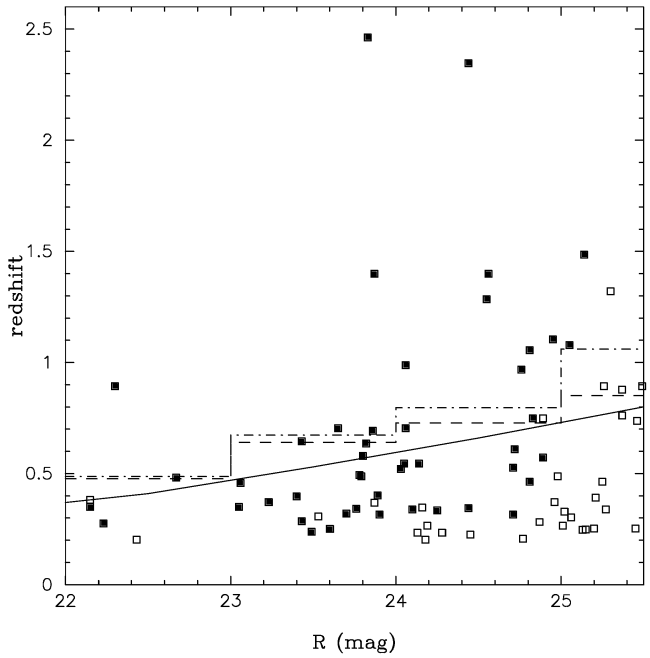

FIG. 11.—Mean redshift vs. intrinsic magnitude for various arclet samples. The solid line represents the no-evolution prediction according to assumptions detailed in the text. The dashed line represents the results for all arclet candidates after making a statistical correction for foreground and cluster contamination. The dot-dashed line is the same sample after excluding images whose isophotal areas are smaller than 50 pixels. Squares represent the individual inverted redshifts of all arclets greater than 50 pixels in area. Filled symbols denote those with $\epsilon > 0.2$, and open symbols those with $\epsilon < 0.2$.

culty when comparing with current model predictions, which are largely based on integrated magnitudes. Either it must be assumed that the compact sources are a representative subset of those for which inversion is practical or evolutionary models must take into account the effect of an areal threshold rather than an integrated magnitude. Conceivably, with much longer integrations, the signal-to-noise ratio of each faint image will improve sufficiently to reduce the uncertainties.

As the source surface brightness and *k*-corrections depend strongly on redshift, the visibility of a faint source is also a complex function of redshift and type. Although this is true of any isophotally selected faint galaxy sample and is not further distorted by the lensing process, as the arclet population presumably probes to much higher redshift than the brighter spectroscopic samples, the uncertainties in allowing for visibility losses are presumably much greater. A specific problem, raised originally by Smail et al. (1991), is the possibility that only dense star-forming regions have sufficient ultraviolet flux and high enough surface brightness to produce arclets visible with *HST*.

We now illustrate the above effects in the context of the actual Abell 2218 catalog. To $R \simeq 25$, we have 235 candidate arclets, and for each of these, our procedure delivers a likelihood distribution for the true, unlensed apparent magnitude $R_{\rm source}$ and the redshift z. We can apply the contamination correction discussed in § 4.3.2 to determine the mean redshift of those sources with $z > z_{\rm cl}$, and this can be compared with various predictions. This method is illustrated on the $R_{\rm source}$-z plane in Figure 11 together with the no-evolution prediction for an *R*-limited sample, following the procedure described by Ellis (1996). The latter prediction is based on type-dependent b_J luminosity functions and morphological proportions observed for the local field population (Loveday et al. 1992) transformed to the *R* band using Hubble sequence colors with *k*-corrections taken from King & Ellis (1985). The results are also summarized in Table 4.

For $R < 22$, there are too few arclets in our catalog for meaningful results, but for $22 < R < 25$, the results indicate a gradual increase in mean redshift with apparent magnitude (Fig. 11, *dashed line*). The mean redshift of the arclet population is reasonably close to the no-evolution expectations to $R \simeq 24$. However, upon examination of the individual redshifts, there appears to be an excess of low-redshift arclets whose proportion is independent of magnitude and whose origin could explain the trend toward low mean redshifts for faint arclets found earlier by Smail et al. (1996) and Kneib et al. (1994a). It is now clear, following the discussion above, that this effect arises because a fraction of the images have insufficient shear to be correctly inverted, and the residual uncertainties in the correction illustrated in Figure 11 can affect the results at the level at which interesting scientific conclusions are required. We can quantify this effect by restricting the technique to those images whose isophotal areas exceed 50 pixels and whose ellipticity is larger than 0.2. As Figure 11 shows (*dot-dashed line*), this leads to an increase in the mean redshift at all magnitudes, and the large majority of the "low z" points disappear.

Out of a total sample of 42 well-defined arclets to $R \simeq 25.5$, only two are beyond $z \simeq 2$, and the mean redshift at $R \simeq 25$ is $\simeq 1$, i.e., only slightly above the no-evolution prediction. Thus, unless the smaller arclets represent an entirely different population of sources or the intrinsic size of a source is a strong function of redshift beyond $\simeq 1$, the absence of a large number of very distant luminous sources to $R \simeq 25$ is a secure result.

It is important to recognize that, for a lensing cluster at $z = 0.175$, Figure 8*b* shows that the mean error in inverted redshift is high even for a well-defined arclet. Typically, for the arclets amenable to individual inversion, $\Delta\epsilon/\epsilon \simeq 0.05$–0.1, and thus, from Figure 9*b*, a source at $z \simeq 2$ could be placed anywhere in the range $1 < z < 3$. A large sample size obviates the need for more precise inversion, but we also note that the redshift distribution would be verified via inversion through a well-constrained cluster at higher redshift. An arclet sample viewed through a cluster at $z \simeq 0.3$ would reduce the implied redshift error for a source at $z \simeq 2$ by a factor of 2. Such a work is now possible with the recently acquired images of the AC 114 cluster.

Finally, we turn to the effect on the inversion of our improved *HST*-based mass model compared to the earlier ground-based equivalent of Kneib et al. (1995). In Table 4,

TABLE 4

INVERSION RESULTS USING ALL ARCLETS

R	$\langle z\rangle_{\rm NE}$	$N^{\rm total}_{\rm arclet}$	$N^{\rm corr}_{\rm arclet}$	$\langle z\rangle_{\rm old}$	$\langle z\rangle_{\rm new}$	$\langle z\rangle^{\rm nocorr}_{\rm new}$
22–23.....	0.41	11	8	0.49	0.49	0.43
23–24.....	0.53	28	26	0.57	0.68	0.65
24–25.....	0.66	31	31	0.64	0.83	0.83

NOTES.—Here $\langle z\rangle_{\rm NE}$ represents the mean expected for no luminosity evolution. $N^{\rm total}_{\rm arclet}$ is the total number in each subsample, and $N^{\rm corr}_{\rm arclet}$ is that after correction for contamination by unlensed images; $\langle z\rangle_{\rm old}$ and $\langle z\rangle_{\rm new}$ represent, respectively, the mean arclet redshift using the ground-based (Kneib et al. 1995) and *HST*-based mass models. For the *HST* model, $\langle z\rangle^{\rm nocorr}_{\rm new}$ indicates the mean redshift prior to contamination correction.

we show the mean inverted redshift after statistical correction for contamination for the ground-based ("old") and *HST*-based ("new") mass models. In both cases, the differences are very minor and illustrate that, although our mass model is certainly not *uniquely* defined, the uncertainty in inversion through Abell 2218 is most likely satisfactorily small.

How might the model be further constrained? The next step will be to verify the inverted redshifts for the brighter arclets spectroscopically, and this will clearly lead to further improvements. Such attempts can be made more effective by selecting the bluest cases with predicted redshifts $z \leq 2$, where strong emission lines would lie in the range of optical and near-infrared spectrographs. A subset of well-distributed arclets would represent a valid test of our inversion since this depends on geometrical quantities and the cluster mass model, both of which are independent of the photometric properties of the background sources. As an encouragement for interested workers, we therefore list in Table 2 the inverted redshifts for each of the major arcs and multiple images discussed in § 2.3, and those remaining arcs for which reliable inversion is possible are plotted on Figure 11.

Although inversion through well-constrained lenses is an extremely promising prospect, this pilot study suggests that an important observational limitation in our study is the signal-to-noise ratio of the required shape parameters for the faint sources. This demonstrates the importance of securing deeper *HST* exposures. A second revelation is the importance of developing a new approach in the construction of model predictions. It seems unlikely that such faint sources can easily be constructed into apparent magnitude–limited samples, and thus much work is needed to produce surface brightness–limited predictions. Finally, one would like to observe a larger angular coverage (e.g., with multiple *HST* pointings) to be able to better constrain the mass distribution by using both weak shear technique and multiple images, and therefore having a larger number of faint galaxies to determine their redshift distribution. Notwithstanding these difficulties, Abell 2218 remains an exceptionally promising cosmic lens, and the opportunities for verifying or otherwise the predicted redshifts for the brighter arclets are excellent. Such data will improve the mass model and lead to even tighter constraints on the redshifts of sources beyond reach of ground-based spectrographs.

6. CONCLUSIONS

The *HST* image of Abell 2218 has not only confirmed with impressive precision the original mass model of Kneib et al. (1995) but also allowed us to see the promise that lensing inversion holds in constraining the properties of large numbers of distant galaxies.

We summarize our conclusions as follows:

1. We have attempted to constrain the redshift distribution of very faint galaxies by using *HST* to study images of sources that have been lensed by a massive foreground cluster. Using multiple images and newly discovered lensing features in the rich cluster Abell 2218, we have constructed a precise mass distribution that is more tightly constrained than that for any other cluster. With *HST* high-resolution data, we have now sufficient information to constrain not only the mass profile of the cluster but also to obtain limits on the masses of individual cluster galaxies.

2. We have developed a new formalism for this inversion that is based on the observed image parameters of faint sources. We demonstrate how it is possible to deduce the redshift distribution of very faint galaxies viewed through the cluster as well as to account statistically for contamination by unlensed sources. First results are presented for a large sample of arclets to $R \simeq 25$–25.5, about 3 mag fainter than results from ground-based spectroscopy.

3. We discuss limitations that arise in the interpretation of redshift distributions derived through lensing inversion. These may help explain why earlier results tended to yield redshift distributions less than extrapolation of ground-based spectroscopy would imply. Even with *HST*, it is difficult to measure faint galaxy shapes adequately to invert magnitude-limited samples. More robust results are obtained by using area-limited samples.

4. We demonstrate that, notwithstanding the uncertainties and sample selection criteria we have adopted, the absence of a large number of very distant sources ($z > 2$) in our inverted redshift distributions is a secure result. At $R \simeq 25$, the mean redshift for samples corrected for contamination or those based on individual arclets of high signal-to-noise ratio is only $\simeq 0.8$–1.2.

5. The brighter arclets, whose redshifts are estimated via our technique, are amenable to direct spectroscopic examination. Such attempts can be made more effective by selecting the bluest cases with predicted redshifts $z \leq 2$, where strong emission lines would lie in the range of optical and near-infrared spectrographs. Note that confirmation of a carefully selected subset of well-distributed arclets would still represent a valid test of our inversion technique, which depends only on geometrical quantities and the cluster mass model, both of which are independent of the photometric properties of the background sources.

We thank Bob Williams and Ray Lucas and other STScI staff for their assistance with the rapid processing of this data. We acknowledge enthusiastic support from a number of colleagues, including Roger Blandford, Bernard Fort, Yannick Mellier, Jerry Ostriker, Roser Pelló, Peter Schneider, and Martin Rees. This paper is based on observations with the NASA/ESA *Hubble Space Telescope*, obtained at the Space Telescope Science Institute, which is operated by the Association of Universities for Research in Astronomy, Inc. J.-P. K. gratefully acknowledges support from an EC Fellowship, and I. S. from NATO and Carnegie Fellowships. W. J. C. acknowledges support from the Australian Department of Industry, Science, and Technology, the Australian Research Council, and Sun Microsystems.

REFERENCES

Bertin, E. 1994, Ap&SS, 217, 4
———. 1995, SEXTRACTOR Manual (Paris: IAP)
Bertin, E., & Arnouts, S. 1996, A&AS, 117, 393
Birkinshaw, M., & Hughes, J. P. 1994, ApJ, 420, 33
Bonnet, H., & Mellier, Y. 1995, A&A, 303, 331
Brainerd, T., Blandford, R., & Smail, I. 1996, ApJ, 466, 623
Ebbels, T. M. D., Kneib, J.-P., & Ellis, R. S. 1996, in preparation
Ellis, R. S. 1996, in Unsolved Problems in Astrophysics, ed. J. N. Bahcall & J. P. Ostriker (Princeton: Princeton Univ. Press), in press
Fort, B., & Mellier, Y. 1994, A&A Rev., 5, 239
Griffiths, R. E., et al. 1994, ApJ, 435, L19
Holtzman, J. A., Burrows, C. J., Casterno, S., Hester, J. J., Trauger, J. T., Watson, A. M., & Worthey, G. 1995, PASP, 107, 1065
Jones, M., et al. 1993, Nature, 365, 320

Kaiser, N., Squires, G., & Broadhurst, T. 1995, ApJ, 449, 460
Kassiola, A., & Kovner, I. 1993, ApJ, 417, 450
King, C. R., & Ellis, R. S. 1985, ApJ, 288, 456
Kneib, J.-P. 1993, Ph.D. thesis, Univ. Paul Sabatier, Toulouse, France
Kneib, J.-P., Mellier, Y., Fort, B., & Mathez, G. 1993, A&A, 273, 367
Kneib, J.-P., Mellier, Y., Fort, B., Soucail, G., & Longaretti, P. Y. 1994a, A&A, 286, 701
Kneib, J.-P., Mellier, Y., Pelló, R., Miralda-Escudé, J., Le Borgne, J.-F., Böhringer, H., & Picat, J.-P. 1995, A&A, 303, 27
Kneib, J.-P., Melnick, J., & Gopal-Krishna. 1994b, A&A, 290, L25
Kochanek, C. S. 1990, MNRAS, 247, 135
Le Borgne, J.-F., Pelló, R., & Sanahuja, B. 1992, A&AS, 95, 87
Loveday, J., Peterson, B. A., Efstathiou, G., & Maddox, S. J. 1992, ApJ, 390, 338
Mellier, Y., Fort, B., & Kneib, J.-P. 1993, ApJ, 407, 33
Pelló, R., Le Borgne, J.-F., Sanahuja, B., Mathez, G., & Fort, B. 1992, A&A, 266, 6
Pelló, R., Soucail, G., Sanahuja, B., Mathez, G., & Ojero, E. 1988, A&A, 190, L11
Saraniti, D. W., Petrosian, V., & Lynds, R. 1996, ApJ, 458, 57
Schneider, P., Ehlers, J., & Falco, E. E. 1992, Gravitational Lenses (Berlin: Springer)
Smail, I., Couch, W. J., Ellis, R. S., & Sharples, R. M. 1995a, ApJ, 440, 501
Smail, I., Dressler, A., Kneib, J.-P., Ellis, R. S., Couch, W. J., Sharples, R. M., & Oemler, A., Jr. 1996, ApJ, 469, 508
Smail, I., Ellis, R. S., Fitchett, M. J., Norgaard-Nielsen, H. U., Hansen, L., & Jorgensen, H. E. 1991, MNRAS, 252, 19
Smail, I., Hogg, D. W., Blandford, R., Cohen, J. G., Edge, A. C., & Djorgovski, S. G. 1995b, MNRAS, 277, 1
Smail, I., Hogg, D. W., Yan, L., & Cohen, J. 1995c, ApJ, 449, 15
Wilson, G., Cole, S., & Frenk, C. S. 1996, MNRAS, 280, 199